JOURNAL OF PETROLOGY | VOLUME 51 | NUMBERS 1 & 2 | PAGES 185–200 | 2010 | doi:10.1093/petrology/egp089

Trapped Melt in the Josephine Peridotite: Implications for Permeability and Melt Extraction in the Upper Mantle

M. SUNDBERG[1]*, G. HIRTH[1] AND P. B. KELEMEN[2]

[1]DEPARTMENT OF GEOLOGICAL SCIENCES, BROWN UNIVERSITY, 324 BROOK ST., PROVIDENCE, RI 02912-1846, USA
[2]LAMONT DOHERTY EARTH OBSERVATORY, COLUMBIA UNIVERSITY, 61 ROUTE 9W, PO BOX 1000, PALISADES, NY 10964-8000, USA

RECEIVED FEBRUARY 12, 2009; ACCEPTED NOVEMBER 25, 2009
ADVANCE ACCESS PUBLICATION JANUARY 15, 2010

Tabular dunites in the Josephine peridotite of southwestern Oregon represent conduits for melt extraction from the upper mantle. The amount of melt trapped within these channels during cooling and exhumation of the peridotite massif was calculated using a mass-balance approach. These calculations suggest that no more than 0·1–0·2 vol. % melt could have been trapped within these dunites after crystallization. This observation indicates that the threshold porosity for melt extraction is ≤0·2 vol. %. We use this constraint to evaluate published permeability models for partially molten dunite. We then use constraints from these permeability models to calculate lower bounds on the bulk viscosity of partially molten dunite and conclude that the bulk viscosity is of the order of 10^{23} Pa s at melt contents of ∼0·1 vol. % and reasonable melt extraction column heights. The small amount of trapped melt in these dunites is consistent with geochemical evidence for near fractional melting in the upper mantle.

KEY WORDS: *mantle; ophiolite; partial melting; peridotite*

INTRODUCTION

The mechanism of melt extraction from the upper mantle at oceanic spreading centers, plumes, and subduction zones influences a wide range of geophysical and geochemical phenomena. The efficiency of melt extraction controls the extent to which mantle melting is fractional (Iwamori, 1993*a*, 1993*b*; Kelemen *et al.*, 1997). This affects the bulk composition, isotope, and trace element systematics of the erupted lavas. Likewise, the physical properties of peridotite are a strong function of intergranular melt fraction (e.g. Roberts & Tyburczy, 1998; Gribb & Cooper, 2000; Hirth & Kohlstedt, 2003). This, in turn, affects the dynamics of mantle upwelling, with localized buoyancy driven flow dominating at high melt fractions, and passive upwelling dominating at low melt fractions (Buck & Su, 1989; Turcotte & Phipps Morgan, 1992; Spiegelman, 1996).

Several lines of geophysical and geochemical evidence can be used to constrain the melt fraction present beneath oceanic spreading centers. Models of melt migration based on geochemistry require near fractional melting where melt begins to separate from its solid residuum at porosities of the order of 0·1% (Johnson *et al.*, 1990; Lundstrom *et al.*, 1995, 2000). Field-based studies of ophiolite bodies provide a complementary method of investigating melt migration processes in the upper mantle. Many ophiolites preserve extensive evidence of partial melting and melt migration. In particular, replacive dunite bodies found in ophiolites have been interpreted as the result of melt migration, and are believed to represent major conduits for melt transport within the shallow upper mantle (e.g. Kelemen *et al.*, 1997). Melt extraction from these channels cannot be perfectly efficient. Given realistic time-scales, two-phase compaction models predict that there is a finite amount of melt that can be expelled out of a peridotite (McKenzie, 1984). Furthermore, depending

*Corresponding author. Present address: Department of Geology and Geophysics, University of Minnesota, 310 Pillsbury Dr. SE, Minneapolis, MN 55455, USA. Telephone: 401-63-932. Fax: (401) 863-2058. E-mail: sundb154@umn.edu

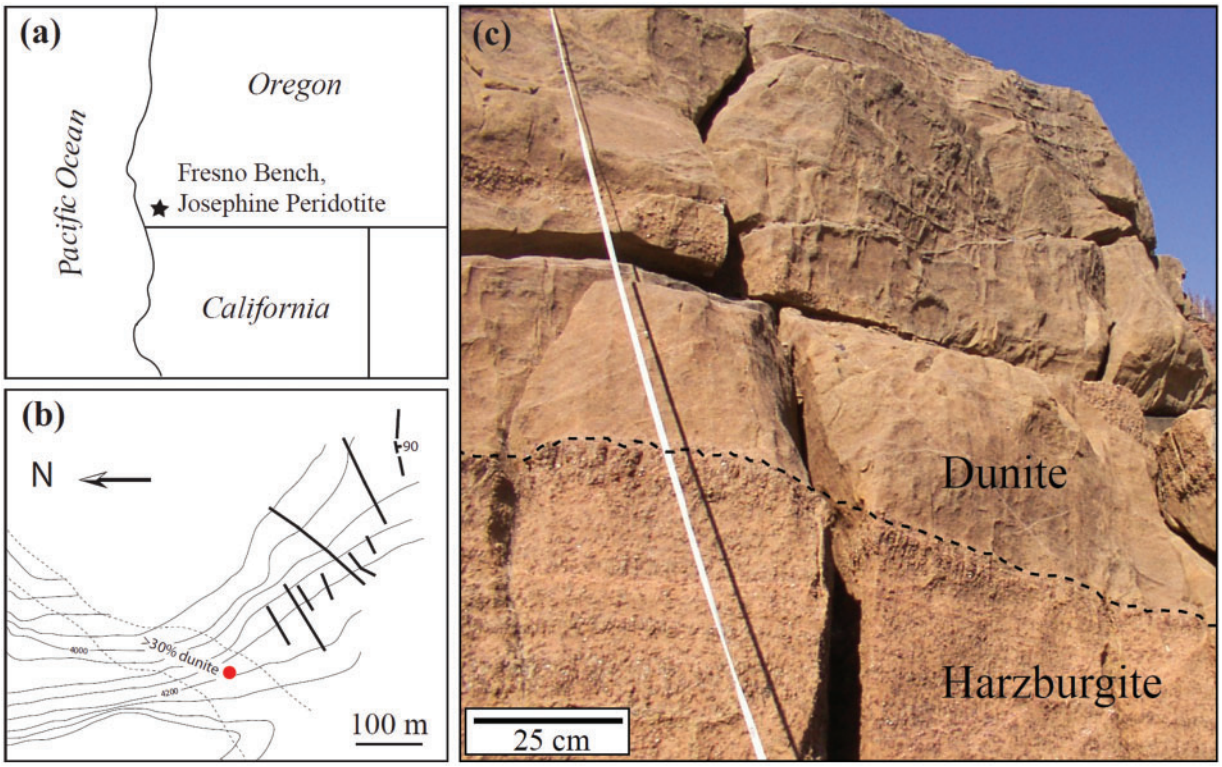

Fig. 1. (a) Location of Josephine peridotite in southwestern Oregon. A detailed geological map of the Fresno bench locality of the Josephine peridotite is shown in (b). The nine samples described in this study were collected across a 13 m transect that trends ESE of a near-vertical dunite shear zone at the location indicated by the red circle. The transect is located within the region bounded by the fine dashed lines and labeled >30% dunite. The continuous lines represent smaller high-temperature mylonitic shear zones (for additional details, see Kelemen & Dick, 1995). The fine lines are contours of elevation with a contour interval of ~15 m (50 ft). (c) Photograph of the contact between the dunite shear zone and the surrounding deformed harzburgite. Dashed line represents the contact between the dunite (above) and the harzburgite (below) at a position 12·9 m along the transect.

on the wetting behavior of the melt, there may be a threshold porosity below which a large percentage of the melt is no longer interconnected and therefore incapable of moving (Nicolas, 1986; Faul, 1997).

In this study we use a mass-balance calculation between the whole-rock chemistry and measured mineral compositions to quantify the small melt fraction that was trapped within a dunite conduit. We refer to any melt, or cumulate crystals derived from that melt, retained by the peridotite during cooling and exhumation as 'trapped melt' for the remainder of the discussion. We use the trapped melt fraction calculations to evaluate the efficiency of melt extraction in partially molten peridotite and to test experimentally and numerically determined permeability models. Additionally, the amount of melt trapped within a peridotite will be related to the threshold porosity required to initiate melt migration following the onset of melting. As outlined below, this value represents a maximum estimate for the minimum porosity during melt extraction.

The Josephine peridotite of southwestern Oregon is ideal for making these measurements (Fig. 1). The Josephine is a partially dismembered ophiolite that probably formed in a Jurassic back-arc basin (Harper, 1984). This peridotite is dominantly harzburgite, but is characterized by numerous replacive dunites (<1% secondary phases), which are often spatially associated with meter-scale shear zones (Loney & Himmelberg, 1976; Kelemen & Dick, 1995). These tabular dunites have been interpreted to form as the result of melt–rock reaction between peridotite and decompressing melt that preferentially dissolves silica-rich orthopyroxene and precipitates olivine (Dick, 1977*b*; Quick, 1982; Kelemen, 1986, 1990). Mass-balance calculations are necessary to calculate the trapped melt fraction because textural evidence and orthopyroxene compositions suggest that the trapped melt fraction within the Josephine peridotite is small (e.g. Dick, 1977*a*). In particular, the almost complete absence of plagioclase and clinopyroxene within any Josephine peridotite samples indicates that nearly all the melt must have been extracted. Furthermore, these dunites allow us to directly compare different permeability models that were derived for single-phase rocks without the potential complications associated with a second solid phase (e.g. Toramaru &

Table 1: Whole-rock XRF compositions (wt %) of the Josephine dunites

	Position along transect (m)								
	0	1·3	4·25	6	11·5	11·85	12·2	12·5	12·9
Sample no.:	3923Z19	3923Z16	3923Z15	3923Z14	3924Z32	3923Z12	3924Z24a	3924Z27	3924Z29a
SiO_2	36·75	37·03	37·91	37·72	37·30	38·15	37·85	37·19	37·14
TiO_2	0·01	0·01	0·01	0·01	0·01	0·01	0·01	0·02	0·01
Al_2O_3	0·11	0·14	0·17	0·07	0·10	0·14	0·12	0·21	0·25
Fe_2O_3	3·39	2·74	2·36	2·43	2·23	2·63	3·23	3·27	2·81
FeO	4·19	4·38	4·75	4·76	5·19	4·91	4·62	4·98	6·08
MnO	0·12	0·12	0·12	0·12	0·12	0·12	0·12	0·13	0·14
MgO	46·73	48·10	47·68	47·66	47·75	48·56	47·28	46·77	46·75
CaO	0·09	0·16	0·14	0·13	0·16	0·19	0·13	0·11	0·16
P_2O_5	0·00	0·00	0·01	0·01	0·01	0·01	0·01	0·01	0·01
NiO	0·37	0·37	0·38	0·38	0·39	0·38	0·37	0·36	0·36
Cr_2O_3	0·29	0·34	0·38	0·23	0·28	0·43	0·27	0·36	0·34
LOI	8·14	7·07	6·59	6·82	6·74	4·65	6·20	6·53	5·68
Total	99·86	100·19	100·27	100·09	100·08	99·92	99·89	99·61	99·46
Fe_2O_{3tot}	8·05	7·61	7·64	7·72	8·00	8·09	8·36	8·80	9·57
FeO_{tot}	7·24	6·85	6·87	6·95	7·20	7·28	7·52	7·92	8·61
Mg-no.	92·0	92·6	92·5	92·4	92·2	92·2	91·8	91·3	90·6

Accuracy of measurements is <5% for TiO_2, <2% for Fe_2O_{3tot}, and <1% for all other oxides used in this study. Measurement precision is better than 1% for all oxides. Details are available at http://www.fandm.edu/x7992.xml. Data originally published by Morgan *et al.* (2008).

Fujii, 1986; Zhu & Hirth, 2003). Finally, the Josephine peridotite is relatively unserpentinized compared with many other peridotite massifs, decreasing the uncertainty in our mass-balance calculations.

METHODS

Nine samples of dunite were collected across a 12 m wide dunite shear zone in the Josephine peridotite for chemical analysis and mass-balance calculations. A map and photograph of this dunite are shown in Fig. 1. Whole-rock compositions were measured via X-ray fluorescence spectroscopy (XRF) at Franklin and Marshall College. The results of these analyses are presented in Table 1. Olivine and spinel compositions were measured using wavelength-dispersive spectroscopy (WDS) on a Cameca SX-100 electron microprobe operating at 20 kV and 25 nA at Brown University. At least eight points in both olivine and spinel were analyzed in each thin section. Single olivine grains are dissected by multiple microcracks associated with serpentinization (Fig. 2). Microprobe points were chosen from the center of continuous grain fragments of olivine; a sampling of these points should represent both core and rims of single grains. Core to rim compositional variation was measured for several spinel grains in one thin section. The results of the analyses for olivine and spinel were previously reported by Morgan *et al.* (2008) and are repeated in Tables 2 and 3, respectively. All iron is expressed as FeO.

The concentrations of TiO_2 and Al_2O_3 in olivine are below the detection limit of the electron microprobe, consequently their abundance was measured using the Cameca IMS-1280 ion microprobe at the Woods Hole Oceanographic Institution. Measurements of $^{27}Al/^{30}Si$ and $^{46}Ti/^{30}Si$ were made using KLB-1 olivine, orthopyroxene, and clinopyroxene as standards (Takahashi, 1986). Five measurements were made in each sample. The measurement techniques are described in detail in the supporting online material (available for downloading at http://www.petrology.oxfordjournals.org/). The data are reported in Table 2.

We calculate the trapped melt fraction within the Josephine dunite using two methods. In the first method, the modal abundances of olivine and spinel were calculated using a non-negative least-squares fit of the measured mineral compositions to the whole-rock XRF results according to the equation

$$c_i = C_{ij}x_j \quad (1)$$

where c_i is a vector whose rows are the concentrations of each oxide in the whole-rock as measured by XRF

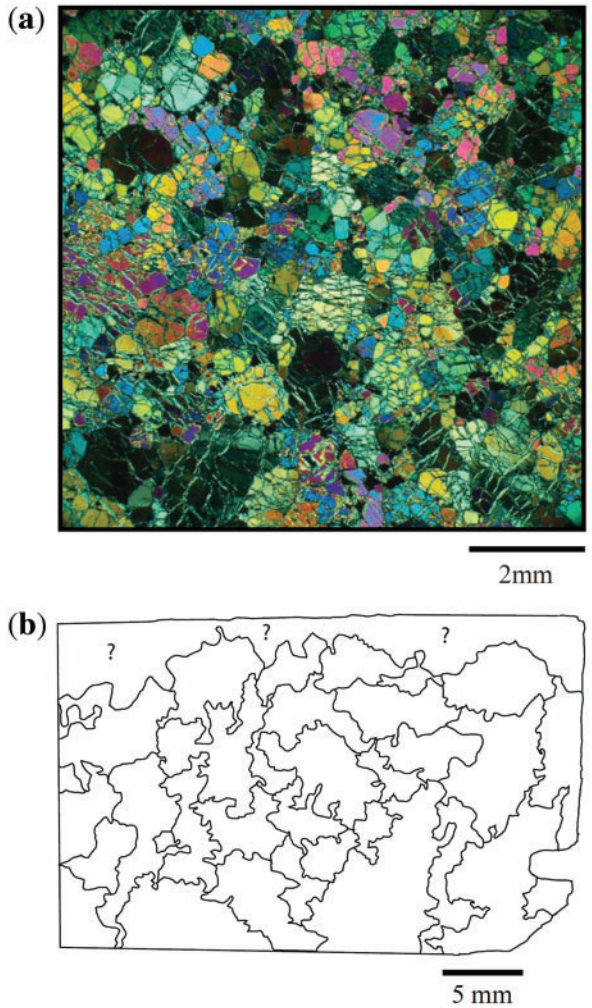

Fig. 2. (a) Photomicrograph (crossed polars) of a dunite sample from the Josephine peridotite taken from position 11·85 m along the transect. The sample is almost entirely composed of olivine. The coarse grain size and pervasive serpentinization should be noted. (b) Tracing of optically continuous olivine grains from a sample taken from position 12·6 m. It should be noted that the grain size, >5 mm, is considerably larger than shown in (a). Both samples are almost entirely composed of olivine, with a very small fraction of spinel.

(Table 1), C_{ij} is a matrix whose rows are the oxide concentrations as measured in each solid phase (Tables 2 and 3) and whose columns are the phases, and x_j is the vector of modes. NiO was excluded from the inversion because it was not measured in three samples. These modal abundances were then combined with measured mineral compositions to calculate the mass of CaO, Al_2O_3, and TiO_2 that could be accounted for within the olivine and spinel that form the dunite. Residual CaO, Al_2O_3, and TiO_2 were then assigned to a melt phase to calculate a weight fraction of trapped melt.

Because spinel dominates the Al_2O_3 and TiO_2 budget of the mineral phases, the estimate of the trapped melt content is very sensitive to the calculated spinel mode. Thus, in the second method, we first calculate the spinel mode based on the abundance of Cr_2O_3 in spinel (because the whole-rock composition of Cr_2O_3 is dominated by spinel). Specifically, we assume that all of the Cr_2O_3 resides in spinel, and then use the measured composition of spinel to calculate a mode. The trapped melt is then estimated from the residual TiO_2 and Al_2O_3 in a manner identical to that discussed above [equation (1)], after subtracting from the whole-rock data quantities of Al_2O_3 and TiO_2 appropriate to a rock with 98 wt % olivine. A similar calculation was performed assuming olivine contains no Al_2O_3 or TiO_2. As discussed below, the results are very weakly sensitive to the assumed olivine mode in these calculations.

All of the calculations are sensitive to the assumed melt composition. For a reference model we use a primitive boninite in equilibrium with Fo_{92} olivine. We choose this composition based on the tectonic setting inferred for the ophiolite (Harper, 1984) and because this composition contains low concentrations of the oxides we use in the mass-balance calculation (thus we provide a conservative estimate for the trapped melt). To avoid inferring an entire melt composition, we fix specific oxides that are most robustly constrained by existing petrological observations; these compositions are similar for any plausible melt composition that could have passed through these dunite channels. CaO was chosen because it behaves incompatibly within a dunite and its abundance within primitive basalt or boninite is well constrained. TiO_2 and Al_2O_3 were chosen because they are comparatively immobile with respect to alteration. We use values of 8 wt % CaO, 12 wt % Al_2O_3, and 0·2 wt % TiO_2 (Hess, 1989). If the melt that passed through these dunite channels was a tholeitic basalt, then the concentration of all three oxides would be larger in the melt, yielding a smaller estimate of the trapped melt content. In the discussion we discuss the role of melt composition on our melt content estimates.

Our mass-balance technique allows us to place an upper bound on the trapped melt content; it does not, however, allow us to place a lower bound. Presumably, crystallization occurred progressively as the peridotite cooled. Thus, the small amounts of CaO, TiO_2, and Al_2O_3 that remain unaccounted for after the mass balance with the solid phases represent both the melt that was present at the final moment before complete crystallization occurred and cumulate crystals that formed during cooling while the melt was still migrating through the dunite.

RESULTS

Mineral compositions and modes

All dunite samples contain trace amounts of chromian spinel with Cr-numbers ranging from 50 at the edge of the dunite body to 72 in the interior (Table 3). The spinel

Table 2: Average and standard deviation (1σ) of olivine compositions (wt %) from the Josephine dunites

	Position along transect (m)								
	0	1·3	4·25	6	11·5	11·85	12·2	12·5	12·9
Sample no.:	3923Z19	3923Z16	3923Z15	3923Z14	3924Z32	3923Z12	3924Z24a	3924Z27	3924Z29a
SiO_2	41·20	41·28	41·41	41·33	41·40	41·29	41·29	40·87	41·20
	(0·17)	(0·13)	(0·12)	(0·15)	(0·13)	(0·13)	(0·17)	(0·08)	(0·12)
MgO	51·09	51·57	51·55	51·58	51·78	51·15	51·02	50·66	50·01
	(0·09)	(0·09)	(0·18)	(0·25)	(0·12)	(0·11)	(0·16)	(0·14)	(0·10)
FeO	7·53	6·89	6·98	7·06	7·26	7·35	7·54	7·99	8·54
	(0·09)	(0·06)	(0·05)	(0·26)	(0·07)	(0·07)	(0·05)	(0·05)	(0·05)
CaO	0·06	0·13	0·13	0·14	0·13	0·13	0·09	0·10	0·11
	(0·02)	(0·02)	(0·05)	(0·05)	(0·02)	(0·03)	(0·01)	(0·03)	(0·03)
NiO	0·44	—	0·45	—	0·45	—	0·43	0·41	0·40
	(0·01)		(0·01)		(0·01)		(0·02)	(0·01)	(0·01)
MnO	0·12	0·12	0·11	0·12	0·13	0·12	0·13	0·13	0·13
	(0·01)	(0·01)	(0·01)	(0·02)	(0·02)	(0·01)	(0·01)	(0·02)	(0·01)
Cr_2O_3	0·005	0·011	0·011	0·011	0·012	0·009	0·008	0·003	0·001
	(0·005)	(0·006)	(0·004)	(0·01)	(0·004)	(0·005)	(0·006)	(0·007)	(0·001)
Al_2O_3*	56 (30)	113 (65)	176 (65)	97 (14)	173 (28)	51 (13)	71 (12)	104 (44)	165 (107)
TiO_2*	14 (0·7)	14 (2)	17 (3)	16 (2)	22 (23)	12 (0·4)	13 (1)	15 (2)	7 (0·5)
Total	100·45	100·01	100·65	100·25	101·18	100·05	100·52	100·17	100·41
Mg-no.	92·4	93·0	92·9	92·9	92·7	92·5	92·4	91·9	91·3
n	10	15	16	15	10	15	10	9	8

Data previously published by Morgan *et al.* (2008).
*Measured using ion microprobe (ppm), this study (see Supplementary Data).

Table 3: Average and standard deviation (1σ) of spinel compositions (wt %) from the Josephine dunites

	Position along transect (m)								
	0	1·3	4·25	6	11·5	11·85	12·2	12·5	12·9
Sample no.	3923Z19	3923Z16	3923Z15	3923Z14	3924Z32	3923Z12	3924Z24a	3924Z27	3924Z29a
Cr_2O_3	52·11	54·82	52·93	52·94	50·68	53·42	47·51	44·34	39·31
	(0·65)	(0·88)	(0·37)	(0·86)	(1·52)	(0·99)	(1·10)	(1·80)	(1·12)
Al_2O_3	17·62	14·01	16·87	15·57	16·69	14·50	20·16	20·45	25·94
	(0·73)	(0·56)	(0·53)	(0·32)	(1·22)	(0·60)	(0·45)	(4·85)	(0·98)
MgO	10·68	10·88	11·98	10·87	10·35	10·62	11·83	10·55	12·36
	(0·62)	(0·93)	(0·86)	(1·07)	(0·69)	(0·83)	(0·86)	(2·47)	(0·59)
FeO	20·68	19·07	17·50	19·32	21·25	20·25	18·59	23·39	20·14
	(0·86)	(1·59)	(1·33)	(1·56)	(1·16)	(1·33)	(1·48)	(5·64)	(1·10)
TiO_2	0·28	0·32	0·24	0·30	0·29	0·26	0·24	0·31	0·18
	(0·01)	(0·02)	(0·07)	(0·02)	(0·02)	(0·02)	(0·01)	(0·07)	(0·02)
MnO	0·09	0·02	0	0·03	0·02	0·02	0·02	0·06	0·02
	(0·03)	(0·07)		(0·07)	(0·04)	(0·05)	(0·06)	(0·09)	(0·06)
Total	101·46	99·11	99·53	99·05	99·29	99·09	98·37	99·11	97·96
Cr-no.	66·5	72·4	67·8	69·5	67·1	71·2	61·2	59·8	50·4
n	10	10	10	10	10	10	12	10	10

Data previously published by Morgan *et al.* (2008).

grains show some core-to-rim compositional zoning. The Cr-number increases toward the rim along with a corresponding decrease in the Mg-number. Minor depletion in TiO_2 is also observed toward the rims (Fig. 3). The mean abundances of TiO_2 and Al_2O_3 averaged across the diameter of this grain are 0·28 and 14·12 wt % respectively. In comparison, the mean concentration (and standard deviation) of TiO_2 and Al_2O_3 calculated from many grains in this sample is 0·26 (0·02) wt % and 14·50 (0·60) wt % respectively. Olivine grains within the dunite have an Mg-number of ~91 to 93 (Table 2). Al_2O_3 concentrations in olivine range from 50 to 180 ppm, whereas TiO_2 concentrations range from 7 to 17 ppm. Spatial gradients within the studied dunite body in both major and minor elements have been discussed by Morgan *et al.* (2008). Minor elements do not show a systematic trend across the dunite. The least-squares inversion using Method 1 returns a mean olivine mode of 98·3 (0·3) wt % (average of nine samples, 1σ shown in parentheses) and a spinel mode of 1·1 (0·3) wt % (Tables 3 and 4). Using Method 2, we calculate a mean spinel mode of 0·7 (0·1) wt %. Point counting of the spinel abundance in one thin section gave a spinel mode of 0·8 wt % (calculated from ~1000 points and using a density of ~4600 kg/m^3 for spinels of this composition), suggesting that the mode calculated using Method 2 is more accurate. Furthermore, the spinel mode based on Method 1 yields a deficit in chromium and aluminum (see residuals in Table 5). Considering that spinel is the dominant host of these two oxides, this observation also suggests that the spinel mode based on Method 2 is more accurate.

Geothermometry

The equilibrium distribution coefficient of Al_2O_3 between olivine and coexisting spinel is sensitive to both temperature and the Cr-number [100 × molar Cr_2O_3/(Cr_2O_3+Al_2O_3)] of the spinel (Wan *et al.*, 2008). Consequently, we use our measured mineral compositions to calculate a minimum temperature for dunite formation. Application of this geothermometer suggests temperatures ranging from 914 to 1087°C, with a mean and standard deviation of 1001 and 67°C respectively. This temperature estimate is in close agreement with estimates derived from other methods. First, the equilibration temperature of cross-cutting gabbro veins that are spatially associated with the Josephine dunites provides a complementary estimate for the minimum temperature for porous melt

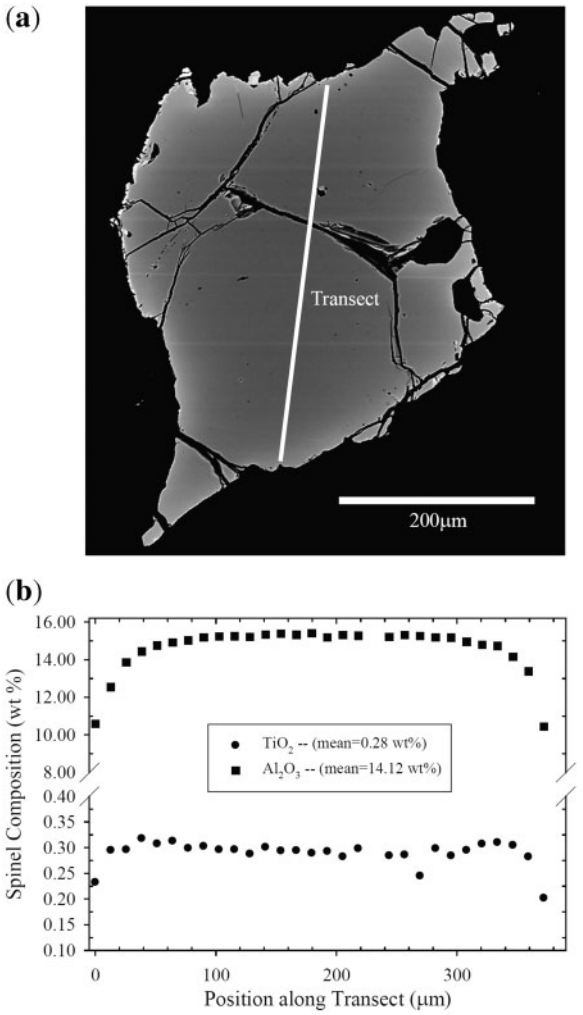

Fig. 3. Compositional profiles of TiO_2 and Al_2O_3 across a spinel grain from position 11·85 m along the traverse. (a) Backscattered electron micrograph of the spinel grain. (b) Variation in TiO_2 and Al_2O_3 across the spinel grain. The concentration gradients are reflected in the gradient in backscatter contrast in (a).

Table 4: Estimates of mean olivine and spinel modes (wt %) from inversion calculations

Inversion method for mineral modes	Oxide used in melt content calculation	Estimate of trapped melt content	Mean spinel mode from inversion	Mean olivine mode from inversion
(1) Entire composition	CaO	0·5	1·1	98·3
	Al_2O_3	<0		
(2) Cr_2O_3 in spinel	Al_2O_3	0·1	0·7	—

Table 5: Results and residuals (wt %) from least-squares fit to entire composition

wt % oxide	Position along transect (m)								
	0	1·3	4·25	6	11·5	11·85	12·2	12·5	12·9
SiO_2	−0·587	−0·932	−0·216	−0·292	−0·549	−0·621	−0·244	−0·312	−0·807
MgO	0·434	0·700	0·132	0·185	0·385	0·475	0·134	0·199	0·585
FeO	0·272	0·349	0·307	0·354	0·388	0·179	0·428	0·323	0·464
CaO	0·041	0·042	0·022	0·002	0·043	0·072	0·052	0·022	0·063
MnO	0·011	0·011	0·022	0·011	0·002	0·012	0·002	0·012	0·023
Al_2O_3	−0·053	−0·018	−0·006	−0·043	−0·079	−0·018	−0·069	0·058	−0·187
Cr_2O_3	−0·179	−0·256	−0·130	−0·155	−0·215	−0·158	−0·171	−0·195	−0·299
TiO_2	0·006	0·005	0·006	0·006	0·005	0·006	−0·006	0·015	0·006
Olivine mode	0·986	0·988	0·987	0·987	0·980	0·984	0·983	0·982	0·976
Spinel mode	0·010	0·011	0·010	0·007	0·010	0·011	0·010	0·013	0·017

Table 6: Spinel mode from least-squares fit to Cr_2O_3 in spinel

Position along transect (m)								
0	1·3	4·25	6	11·5	11·85	12·2	12·5	12·9
0·006	0·007	0·008	0·005	0·006	0·008	0·006	0·009	0·009

migration (Kelemen & Dick, 1995); the Mg-number [100 × molar MgO/(MgO + FeO)] of hornblende indicates a peridotite temperature of 950–1050°C during vein formation. Second, two-pyroxene geothermometry for Josephine harzburgites yields a similar temperature range (Kelemen & Dick, 1995; Skemer *et al.*, 2009).

Trapped melt calculations

The mass-balance calculations indicate that the mean trapped melt content within the Josephine dunites ranges from essentially zero to 0·5% depending on the inversion method (Fig. 4 for Method 1 and Fig. 5 for Method 2). The inversion method where the mineral modes are calculated from the whole-rock composition (Method 1) yields a trapped melt content of ∼0·5% when calculated from mass balance of CaO, $(CaO_{whole\text{-}rock}–CaO_{solids})/CaO_{melt}$. Method 1 yields a trapped melt content of 3·6% when calculated from a mass balance of TiO_2. In contrast, the trapped melt content is <0 when calculated from a mass balance of Al_2O_3 (not shown in Fig. 4), owing to the deficit in both aluminum and chromium described above. There is no correlation between the mineral modes, or mineral chemistry (Mg-number or Cr-number) and the calculated trapped melt content, nor a relationship between the trapped melt content and position within the dunite body, despite the spatial gradients in mineral chemistry.

The inversion method where the spinel mode is calculated from whole-rock Cr_2O_3 (Method 2) yields a trapped melt content of ∼0·1 wt % when the Al_2O_3 hosted by olivine is subtracted from the whole-rock abundance (Fig. 5). If spinel is assumed to be the only solid phase hosting Al_2O_3 in these rocks, then the mass-balance calculation returns a trapped melt content of ∼0·2 wt %. Using Method 2, calculations of the trapped melt content based on mass balance of TiO_2 yield mean values of 4·5% (not shown in Fig. 5); the significance of the large melt content calculated from mass balance of TiO_2 using both methods is discussed further below.

There are several sources of error that could affect our trapped melt calculations. First, the trapped melt contents calculated from mass balance of TiO_2 are in excess of 3% for both inversion methods. The concentration of TiO_2 in the whole-rock measured by XRF is typically 0·01 wt %, thus these very large values are possibly an artefact of the resolution and precision of the XRF data. Second, chemical zoning of olivine and spinel owing to subsolidus re-equilibration could lead to errors in the interpreted mineral compositions at magmatic conditions. Given our microprobe technique, this variation should be contained within the average of the microprobe measurements. Such zoning effects should be minimal owing to the large olivine

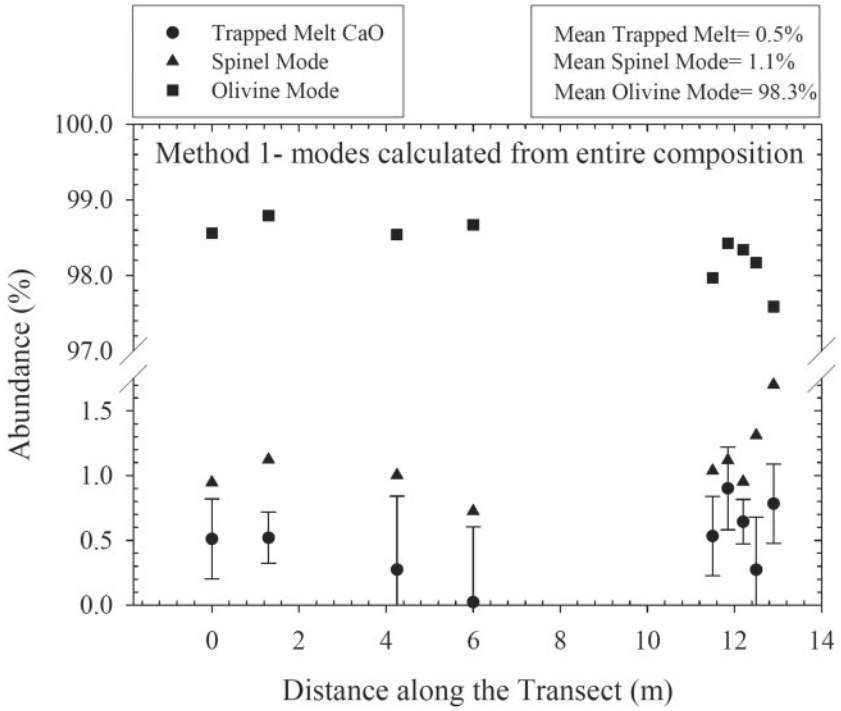

Fig. 4. Plot of the olivine mode, spinel mode and the trapped melt proportion based on the abundance of CaO as a function of position across the dunite shear zone. The error bars on the trapped melt abundance represent the standard deviation of the microprobe measurements. There is no significant variation in trapped melt abundance as function of position within the dunite shear zone.

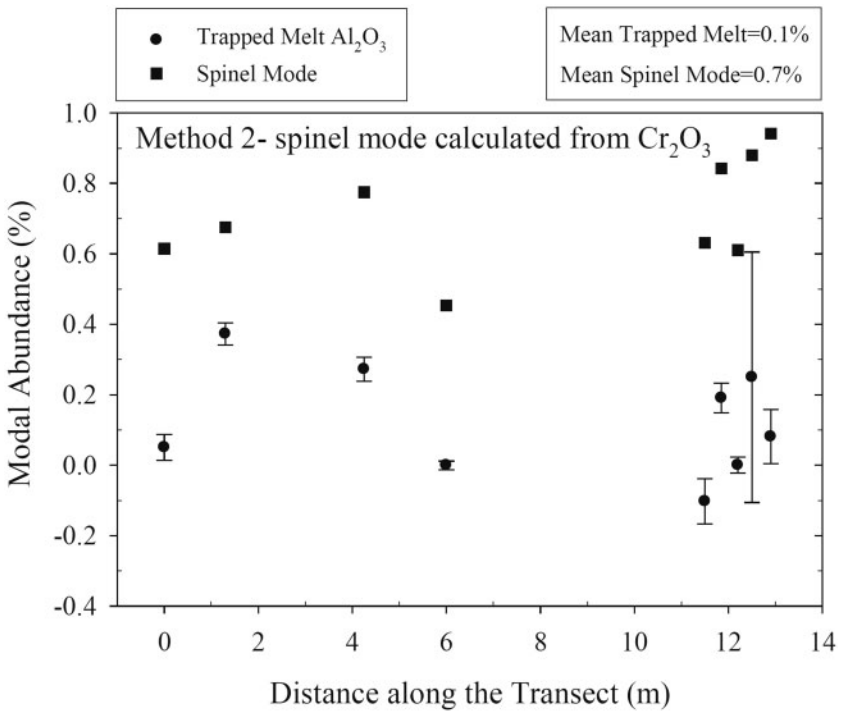

Fig. 5. Plot of spinel mode determined by least-squares inversion of the Cr_2O_3 content of spinels, and the trapped melt proportion based on the abundance of Al_2O_3 as a function of position across the dunite shear zone. The error bars on the trapped melt abundance are based on the standard deviation of the microprobe measurements. There is no significant variation in trapped melt abundance as a function of position within the dunite shear zone.

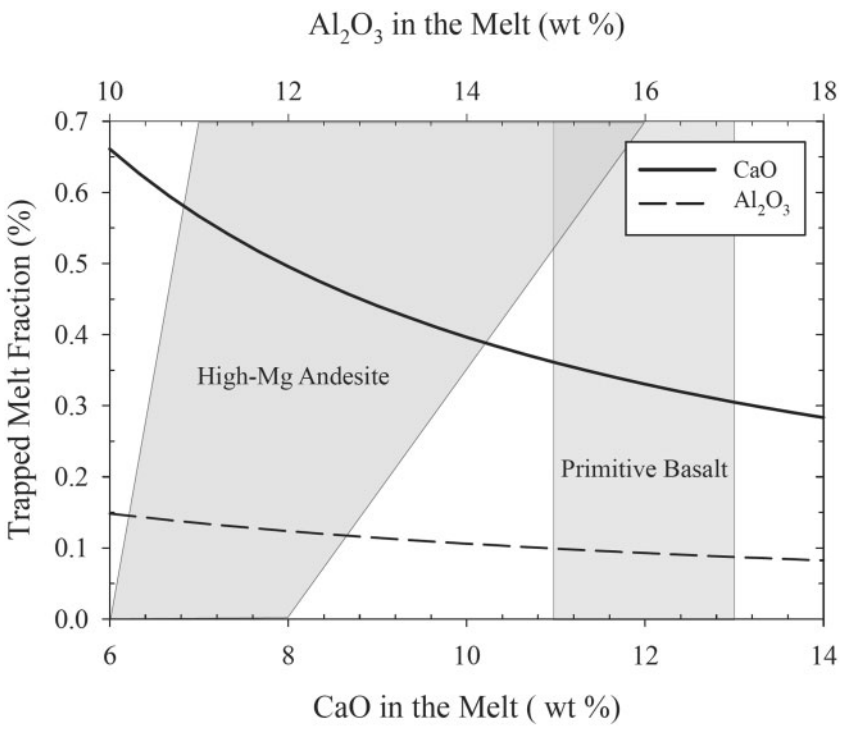

Fig. 6. Plot of the mean trapped melt fraction in the dunites calculated from the two inversion methods over a range of assumed melt compositions. The shaded regions indicate the range of compositions for high-Mg andesite and primitive (Mg-number >65) basalt. For CaO concentrations ranging from 6 to 14 wt %, the mean trapped melt fraction (continuous line) ranges from ~0·6% down to ~0·3%. In contrast, the trapped melt fraction calculated from Al_2O_3 varies over a much smaller range of 0·15% to 0·1% for Al_2O_3 melt contents ranging from 11 to 18 wt %.

grain size. Third, our calculations do not account for the enrichment of incompatible components along olivine grain boundaries (e.g. Hiraga *et al.*, 2003). However, owing to the large grain size of the dunite bodies, the relative volume of grain boundaries is negligible. Fourth, the ubiquitous presence of serpentine indicates that these rocks experienced substantial alteration that could have modified the bulk chemistry. Of the major oxides, the fit to FeO is the poorest (as determined by comparing the ratio of residuals/abundance in Tables 3 and 5); this is due to a source of ferric iron (mostly magnetite) in these rocks as a result of serpentinization. However, there is no correlation between loss on ignition (LOI) in the XRF data and the calculated trapped melt content, suggesting that this problem may not be severe.

The calculated trapped melt contents are sensitive to the assumed composition of the melt that passed through these dunite channels. A plot of the variation of mean trapped melt content with changes in melt chemistry is shown in Fig. 6. The boninite composition that we employ results in more conservative estimates for the trapped melt content. For example, if the melt contained 12 wt % CaO, as characteristic of a primitive basalt (Mg-number >65), then the calculated trapped melt content calculated using Method 1 decreases from 0·5 wt % to 0·3 wt %. The calculations based on Al_2O_3 are much less sensitive to the assumed melt composition than the calculation based on CaO.

In summary, several arguments suggest that the estimate of trapped melt based on Al_2O_3 is the most accurate: (1) its concentration in the whole-rock is less sensitive to post-emplacement alteration than CaO; (2) unlike TiO_2, the concentration of aluminum in the whole-rock is well resolved by XRF; (3) trapped melt contents as large as 0·5% should be easily observed in thin section in the form of plagioclase and clinopyroxene. We therefore conclude that after accounting for the density difference between solid and melt the trapped melt content in these rocks is 0·1 to 0·2 vol. %.

DISCUSSION

Melt extraction from partially molten peridotite is driven by the density contrast between the melt and its solid residuum. The extraction rate is limited by either the rate at which pressure gradients can drive melt expulsion through porous flow or the rate at which the solid can viscously compact and expel melt (Sleep, 1974; Ahern & Turcotte, 1979; McKenzie, 1984; Scott & Stevenson, 1986). Both of

these processes must occur for melt extraction to occur. The rate is limited by the slower process.

Permeability models

In the case where melt extraction is limited by melt flow, the extraction rate is determined by Darcy's Law and therefore dependent on the permeability of the partially molten rock. The permeability of partially molten rock is a function of the grain-scale melt distribution. In texturally equilibrated rocks, melt topology is controlled by the relative interfacial energies of solid–solid (γ_{ss}) and solid–liquid (γ_{sl}) interfaces. As such, the grain-scale melt topology is a thermodynamically determined property that is defined by the dihedral angle (θ):

$$\cos\frac{\theta}{2}=\frac{\gamma_{ss}}{2\gamma_{sl}}. \quad (2)$$

At values of $\theta<60^\circ$, the melt resides at four-grain junctions and along three-grain tubules. The average dihedral angle in the olivine–basalt system is roughly 35°. For these small dihedral angles the melt should be interconnected at all melt contents (see Waff & Bulau, 1979). At higher values of the dihedral angle, small melt fractions will become isolated at four-grain junctions.

The permeability of partially molten rocks where melt occupies three or four-grain junctions takes the form

$$k_\phi=\frac{d^2\phi^n}{C} \quad (3)$$

where d is the grain size, ϕ is the melt fraction, and C is a numerical constant. Numerical simulation of a microstructure with these properties yields $n=2$ and $C=1600$ (Von Bargen & Waff, 1986). Experimental studies of permeability in quartz–brine aggregates yield a permeability relationship with the form of equation (3); however, in the experimental case $n=3$ and $C=270$ (Wark & Watson, 1998). These data are also consistent with measurements of compaction rates in olivine–basalt aggregates at melt fractions in the range of 0·05–0·20 (Renner *et al.*, 2003). At modest melt fractions ($\phi\approx0{\cdot}01$), the experimentally calibrated relationship yields permeabilities roughly an order of magnitude lower than the numerical calculation.

Strictly, the numerical model is valid only when the dihedral angle is single-valued and the sample contains a single grain size. The ubiquitous presence of faceted crystals in texturally mature partial melts demonstrates that the dihedral angle is not single-valued (e.g. Cooper & Kohlstedt, 1982; Waff & Faul, 1992; Jung & Waff, 1998). Consequently, the discrepancy between the two models may be due to (1) anisotropic interfacial energies that alter the melt distribution in three-grain tubules and potentially at four-grain nodes, and (2) a non-uniform grain size that concentrates melt around small grains to maintain constant pore-wall curvature (Wark & Watson, 2003).

Microstructural analyses of olivine–basalt systems suggest that ~85% of the melt in partially molten dunite samples resides in disk-shaped pores (Faul *et al.*, 1994). Faul (1997) argued that this melt distribution yields a permeability relationship fundamentally different from equation (2). Specifically, Faul (1997) predicted a threshold porosity below which disk-shaped melt pockets remain isolated, and that only the remaining ~15% of the melt that resides in triple junction tubules contributes to the permeability described by equation (3). Thus the permeability remains extremely low until the melt fraction exceeds a critical value of $\phi\approx0{\cdot}02$ above which the permeability increases by as much as nine orders of magnitude. In contrast, Wark *et al.* (2003) conducted a similar study on olivine–basalt aggregates and concluded that the melt topology in their samples did not resemble disk-shaped inclusions, but rather was similar to the liquid topology observed in their earlier quartz–brine aggregates.

At the small melt fractions appropriate to the Josephine peridotite, the permeability calculated for the peridotite with the models reviewed above varies by nearly four orders of magnitude. The permeability for each model as a function of melt fraction, evaluated at a grain size of 1 cm, is shown in Fig. 7. For $\phi=0{\cdot}2\%$, the Wark & Watson model yields a permeability of roughly 3×10^{-15} m^2, the Von Bargen & Waff model yields $2{\cdot}5\times10^{-13}$ m^2, and the Faul model yields $1{\cdot}4\times10^{-17}$ m^2.

Each of the three permeability models discussed above was developed for partially molten rocks subject to a hydrostatic state of stress. However, experimental evidence suggests that the melt topology in partially molten rocks is influenced by shear deformation (Zimmerman *et al.*, 1999; Holtzman *et al.*, 2003). In these experiments, melt pockets become elongated in a direction subparallel to the shear plane and may segregate into melt-rich bands of similar orientation, leading to an anisotropic permeability within the partially molten dunite. Furthermore, anisotropic solid–liquid interfacial energies (γ_{sl}) in the olivine–basalt system result in preferential wetting of (010) planes (Jung & Waff, 1998; Zimmerman *et al.*, 1999). As a result of shear deformation in the dunite shear zone, olivine (010) planes preferentially lie subparallel to the shear plane (Kelemen & Dick, 1995). Consequently, shear deformation and anisotropic wetting suggest that the permeability of the dunites of the Josephine peridotite could have been somewhat larger along the shear direction (the present-day vertical, parallel to the dunite–harzburgite contact) than perpendicular to it.

Melt extraction time and velocity

We evaluate each of these permeability models by combining their predictions with melt segregation models and geophysical constraints on the thermal history of the Josephine peridotite to determine which model(s) are consistent with the trapped melt fraction calculations.

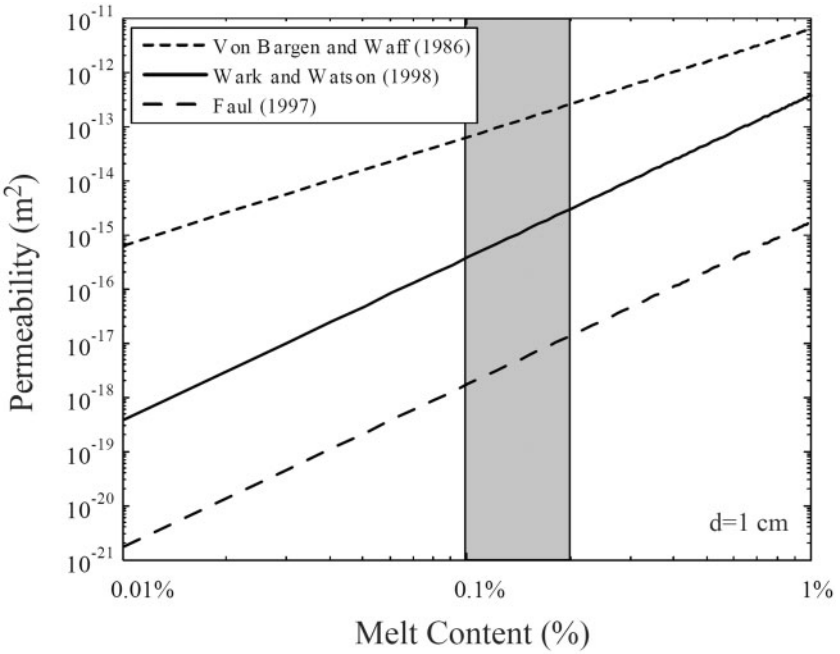

Fig. 7. Plot of permeability vs melt content (%), evaluated at a grain size of 1 cm, for each of the three permeability models. The shaded box indicates the range of melt fractions we calculate for the dunites of the Josephine peridotite. At melt fractions greater than 1–2%, the threshold permeability model predicts an abrupt, ~9 order of magnitude, increase in permeability.

When melt expulsion is limited by melt flow, the extraction of melt is governed by the melt viscosity (μ), the density contrast between solid and melt ($\Delta\rho$), and the permeability (k). In this case, the time-scale required to extract all but 1/e of the initial melt fraction is given by

$$t_h = \frac{h\mu\phi}{k_\phi \Delta\rho g} \tag{4}$$

where g is the acceleration due to gravity and h is the thickness of the layer from which the melt is extracted (McKenzie, 1989). Equation (4) is a statement of conservation of momentum, where melt flow driven by an applied pressure gradient is resisted by Darcy flow of the fluid. Similarly, the velocity (v) of melt flow relative to its solid residuum can be calculated according to Darcy's Law:

$$v = \frac{k_\phi \Delta\rho g}{\mu\phi}. \tag{5}$$

McKenzie (1989) originally used these equations to estimate the volume fraction of melt present in the asthenosphere. For example, with $t_h = 1$ Ma, $h = 40$ km, $\mu = 10$ Pa s, $n = 2$, $C = 3000$, and $\Delta\rho = 500$ kg m^{-3}, he arrived at a melt fraction of 0·0075.

Our upper bound estimates on the trapped melt fraction within the dunite body allow us to invert equation (3) to evaluate the three permeability models shown in Fig. 7. We place a bound on the melt extraction time-scale by considering conductive cooling of oceanic lithosphere. Geobarometry in spatially associated gabbro veins from the Josephine peridotite suggests that it equilibrated at a pressure of 0·5 GPa, or roughly 15 km depth (B. deMartin, personal communication; 2003). Consequently, if the mantle potential temperature was 1350°C, then peridotite at this depth could have remained above its solidus (1000–1100°C for water-saturated boninite) for no more than 2–3 Myr, assuming conductive cooling of a half-space (Turcotte & Schubert, 2002).

Having established a bound on the melt segregation time, we evaluate each permeability model against equation (4) for a range of melting column heights using our calculated melt fraction of $\phi = 0{\cdot}001$–$0{\cdot}002$ and a grain size of $d = 1$ cm as appropriate for the dunites of the Josephine peridotite. As illustrated in Fig. 8, our calculations show that the numerically calculated permeability relationship of Von Bargen & Waff (1986) can produce melt contents of 0·1–0·2% at any melt extraction height. The experimentally determined permeability relationship of Wark & Watson (1998) can yield these small melt contents in less than 2–3 Myr if the melting column height is less than ~10–20 km. If a grain size of 3 cm is used, then these small melt contents are attained in less than 1 Myr, even for melting column heights of 100 km. This observation indicates that permeability determined from fine-grained experimental samples with relatively large melt fractions can be extrapolated to conditions in the Earth with much smaller melt fractions and much coarser grain

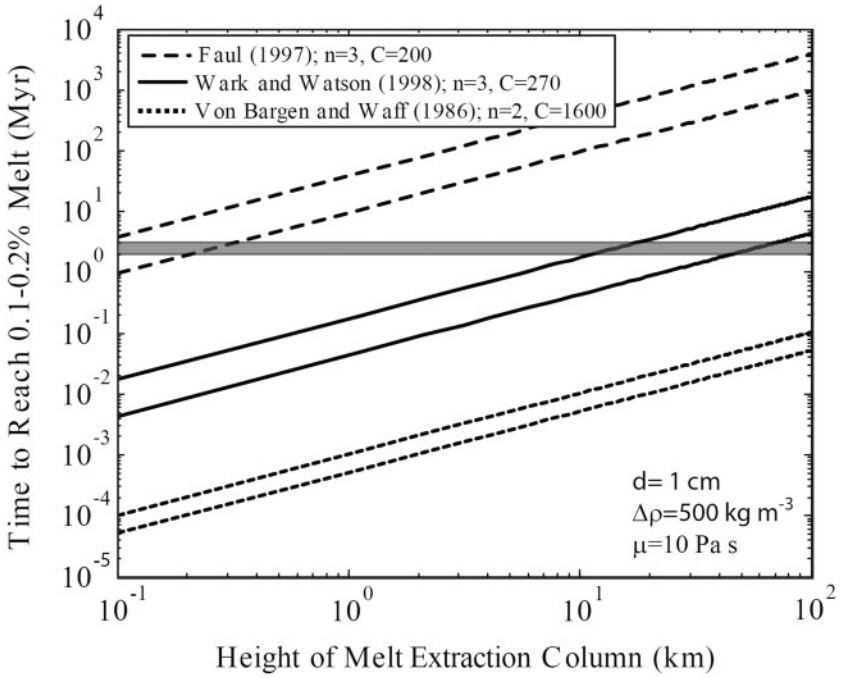

Fig. 8. Plot of the time to reach 0·1–0·2 vol. % melt versus the height of the melting column according to equation (4) for each of the three permeability models. The shaded horizontal line represents a cooling time of 2–3 Myr. The permeability model of Von Bargen & Waff (1986), shown by the short-dashed line, can yield these low melt fractions regardless of the height of the melting column. The experimentally determined permeability model of Wark & Watson (1998) can yield these melt fractions if the melt column is less than ~10–50 km high. In contrast, the threshold permeability model of Faul (1997) cannot yield these low melt fractions unless the melting column is less than a few hundred meters high.

sizes. Differences in the assumed grain size and melt viscosity will influence these relationships following equations (3) and (4). For example, an increase in the melt viscosity associated with conductive cooling would increase the time required to reached $\phi = 0{\cdot}001$–$0{\cdot}002$ and thus diminish the range of melt extraction column heights sufficiently small to yield $\phi = 0{\cdot}001$–$0{\cdot}002$ in less than 2–3 Myr. Similarly, if the trapped melt content is lower than our upper bound estimate, then the permeability reduction associated with equation (3) would also yield longer times and a small range of melt extraction heights.

In contrast, the permeability predicted for the threshold model of Faul (1997) is too small to allow compaction to a melt fraction of ~0·001–0·002 with column heights more than a few hundred meters (Fig. 8). Even if the initial melt fraction upon the cessation of melt production was above the disk-interconnection threshold level [$\phi \approx 0{\cdot}02$ given by Faul (1997), 0·01 given by Faul (2001), where the permeability is $\sim 1 \times 10^{-10}$ m^2], the melt fraction would fall below the threshold porosity in less than 100 years and melt extraction rates would subsequently be limited by the low-permeability regime. In this case, melt extraction from a 15 km high column would require ~150 Myr to reach $\phi = 0{\cdot}002$, which is inconsistent with our analysis.

We suggest the following explanation for the apparent discrepancy between the permeability models of Wark & Watson (1998) and Faul (1997). Although the microstructural analysis of Faul *et al.* (1994) indicates that most triple-junction channels have planar 'fins' extending along two-grain boundaries, it is possible that the majority of the melt within these overall 'disc-like' features lies in the triple-junction region. Thus, although the small aspect ratio of the melt pocket may significantly influence the elastic and viscous creep properties of the aggregate, the transport properties would still be dominated by the relatively large fraction of melt that resides in the three grain tubules (with and without fins extending along two-grain boundaries)—consistent with the microstructural analysis of Wark *et al.* (2003). The increase in surface area to volume ratio resulting from the presence of melt fins will produce a minor decrease in the permeability as a function of melt fraction relative to that predicted by the numerical model of von Bargen & Waff (1986).

Melt migration velocity

Using the same constants as above, we calculate a final melt extraction velocity of roughly 2 cm/yr at $\phi = 0{\cdot}2\%$ using the permeability model of Wark & Watson (1998). The model of Von Bargen & Waff (1986) yields a final melt extraction velocity of slightly below 200 cm/year. The difference between these two models is due to the porosity

exponent in the permeability model and the extrapolation to low porosity.

Bulk viscosity calculations

As mentioned previously, melt extraction requires both melt flow and viscous compaction. The slower of the two processes (i.e. the process with the lower volumetric strain-rate) limits the melt extraction rate. At the very low melt fractions we are discussing, it is possible that a transition from melt-flow limited to compaction limited melt migration occurs. When melt extraction is limited by the viscous compaction rate, the rate of melt extraction is limited by the bulk viscosity (ξ) of the solid. The bulk viscosity relates pressure to volumetric strain-rate ($\dot{\varepsilon}_V$) according to the relationship

$$\xi = \frac{\Delta P}{\dot{\varepsilon}_V} = \frac{\Delta \rho g h}{\dot{\varepsilon}_V}. \quad (6)$$

Our estimate of the trapped melt content can be used to estimate an upper bound for the bulk viscosity of partially molten dunite. We first consider how our estimate of trapped melt content constrains the volumetric strain rate. At low melt fractions, the volumetric strain is nominally equivalent to the change in melt fraction. The volumetric strain rate at the end of melt extraction must be of the order of 0·002/cooling time; the cooling time is no more than the time between when melting stops and when the residue cools below the solidus, which is 2–3 Myr. Therefore, the volumetric strain-rate can be no less than $2 \times 10^{-17}\,\mathrm{s}^{-1}$ (if the compaction rate was significantly smaller, the melt fraction would not decrease to the final value; if the compaction rate was much larger, then all melt would be extracted).

The volumetric strain-rate for melt extraction limited by Darcy flow is given as

$$\dot{\varepsilon}_V = \frac{k \Delta \rho g}{\mu h}. \quad (7)$$

Equation (7) is simply the time derivative of equation (4) after rearranging to solve for ϕ. The volumetric strain rate for melt extraction limited by viscous compaction is given by equation (6). To determine which process is rate-limiting, we introduce a non-dimensional number that scales the volumetric strain-rate of melt extraction rate as a result of fluid flow to the volumetric strain-rate produced by viscous compaction. This expression is given by

$$\beta = \frac{k \xi}{\mu h^2}. \quad (8)$$

Equation (8) suggests that melt extraction is limited by viscous compaction at $\beta > 1$, and by Darcy flow at $\beta < 1$. Equation (8) can be expressed in terms of the compaction length, δ, as $(\delta/h)^2$, originally given by McKenzie (1984) as $\delta = [(4\xi/3 + \eta)k/\mu]^{1/2}$, where η is the shear viscosity of the solid matrix. At these small melt fractions we assume $\xi \gg \eta$ [$\eta \approx 10^{19}$ Pa s after Warren *et al.* (2008)]. The melt extraction column height, h, determines the effective pressure acting on the partially molten column.

In Fig. 9, we plot the results of equation (8) using the permeability calculated from Wark *et al.* (1998) and Von Bargen & Waff (1986) for melt contents of 0·1 and 0·2 vol. %. Assuming a melt extraction column height of 1 km, this 'melt extraction mechanism map' demonstrates that melt extraction is limited by viscous compaction when $\xi > \sim 10^{22}$ Pa s using the Wark & Watson (1998) permeability model and when $\xi > \sim 10^{20}$ Pa s using the Von Bargen & Waff (1986) permeability model. Several important caveats apply to Fig. 9. This bulk viscosity calculation assumes a linear rheology, which may not be strictly applicable to the Josephine dunites. For example, if the melt extraction column height was 1 km, then ΔP is ~5 MPa. At these effective pressures and a relatively coarse grain size ($d = 1$ cm), a non-linear dislocation creep rheology may dominate. Nonlinearity will decrease ξ at larger ΔP, expanding the Darcy flow limited field at the expense of the viscous compaction limited field. Furthermore, ξ will also be temperature dependent. At the low temperatures of the conductively cooling Josephine peridotite (1000–1100°C), the bulk viscosity may be one to two orders of magnitude larger than it is at ~1300°C, given experimentally determined activation enthalpies for creep of olivine aggregates. Finally, at the boundary between the two fields shown in Fig. 9, neither equation (6) nor equation (7) will hold, as neither the melt flow nor the viscous compaction process can be neglected. However, the end-member relationships that we explore here have been observed during experimental studies of melt migration in olivine aggregates (Renner *et al.*, 2003).

Using the constraints from the Josephine dunites, our calculations suggest that the bulk viscosity is significantly larger than the shear viscosity. As illustrated in Fig. 8, the Wark & Watson (1998) and Von Bargen & Waff (1986) models both yield sufficiently high permeabilities to explain the observed melt fraction in the Josephine dunites. Indeed, given our constraints on the thermal history of the Josephine peridotite, Darcy flow of melt should have yielded lower melt fractions than we observe. Consequently, we use the difference between the cooling time (~3 Myr) and the time calculated from equation (3) to constrain the minimum bulk viscosity capable of preventing melt extraction from these dunites for a range of melt extraction column heights (Fig. 10). For a melt extraction column height of ~1 km, the bulk viscosity of the Josephine dunites can be no less than $\sim 10^{23}$ Pa s at temperatures of 1000–1100°C. This value is significantly larger than the shear viscosity inferred for these dunites at identical conditions.

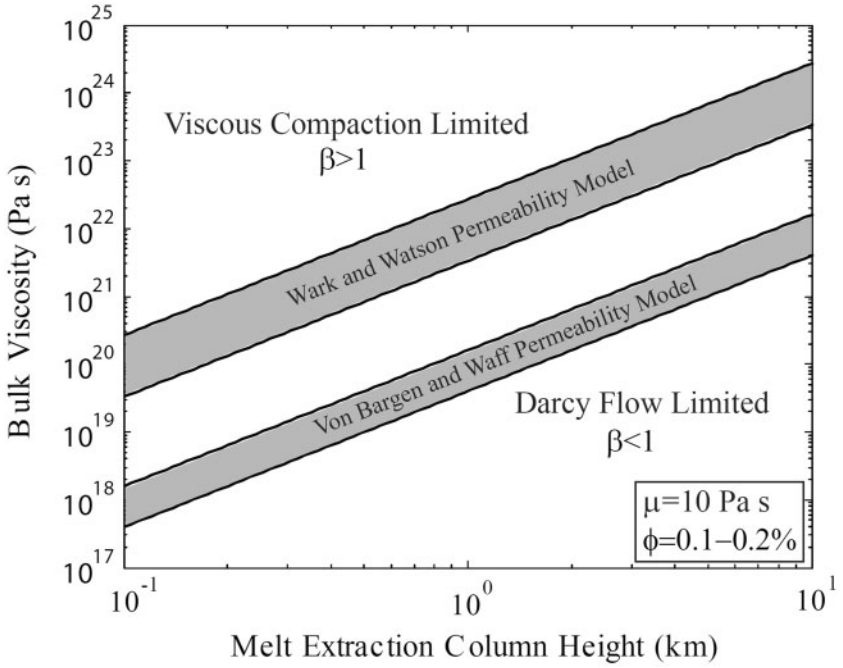

Fig. 9. Melt extraction mechanism map for the dunites of the Josephine peridotite. We evaluate equation (8) against the two permeability models at the small trapped melt fractions associated with the Josephine peridotite. For values above the shaded bands, melt extraction rates in the Josephine should be limited by viscous compaction of the matrix, whereas below the shaded bands it should be limited by Darcy flow of the fluid. For each permeability model, the upper bound represents $\phi = 0{\cdot}001$ and the lower bound represents $\phi = 0{\cdot}002$.

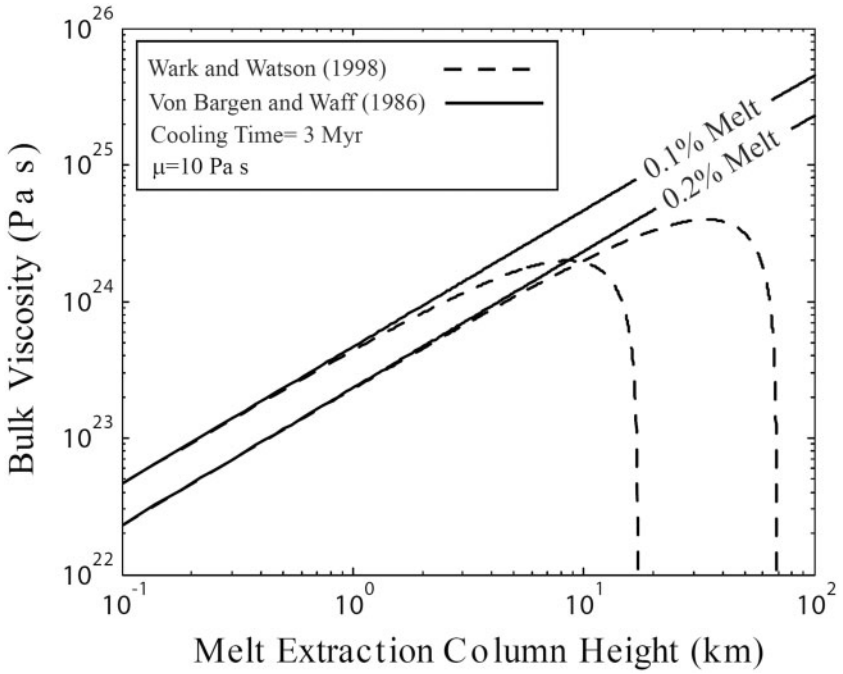

Fig. 10. Lower bound on the bulk viscosity evaluated from the two permeability models calculated from the difference between the cooling time (3 Myr) and the time to reach 0·1–0·2% melt for each permeability model. For a melt extraction column height of 1 km, the bulk viscosity can be no less about 10^{23} Pa s.

As mentioned above, our estimates for the melt fraction represent an upper bound on the trapped melt fraction. A lower melt fraction will have several effects: (1) the estimated Darcy flow segregation time increases, yielding a smaller range of column heights where melt extraction is limited by viscous compaction; (2) the bound on volumetric strain decreases, increasing the estimated bulk viscosity. For example, if our calculated trapped melt content is an order of magnitude too high (0·1–0·2% vs 0·01–0·02%), then the minimum bulk viscosity at a column height of 1 km calculated from the Von Bargen & Waff (1986) permeability model is no less than 10^{24} Pa s. Importantly, it should be noted that the permeability model of Wark & Watson (1998) cannot yield melt fractions of ~0·01 vol. % in 2–3 Myr if the grain size was 1 cm or less.

CONCLUSIONS

We calculate the fraction of trapped melt in dunites from the Josephine peridotite based on mass balance of CaO, Al_2O_3, and TiO_2 and assuming a melt composition appropriate for the tectonic setting. We arrive at trapped melt fractions in the range of 0·1–0·2 vol. %. These calculations indicate that there is not a threshold porosity for melt extraction above 0·1–0·2 vol. %; a lower bound is not constrained. The combination of geophysical constraints on the thermal history of the Josephine peridotite with continuum models of melt segregation suggests that the permeability model of Von Bargen & Waff (1986) provides a sufficiently high permeability to explain the trapped melt fraction in these rocks, regardless of the height of the partially molten column, whereas the permeability model of Wark & Watson (1998) provides a sufficiently high permeability to explain these melt fractions if the partially molten column is less than 10–50 km high. In contrast, the threshold permeability model of Faul (1997) cannot achieve these low melt fractions regardless of the column height. Finally, we use constraints from these permeability models to place bounds on the bulk viscosity during compaction. Our calculations suggest that given reasonable melt extraction column heights, the bulk viscosity of partially molten dunite is no less than ~10^{23} Pa s at these low melt fractions and temperatures.

ACKNOWLEDGEMENTS

We wish to thank Zach Morgan, Yan Liang, and Brian deMartin for assistance with sample collection and microprobe analysis, Carlos Garrido for providing unpublished geochemical data, and Nobumichi Shimizu for assistance with ion microprobe analysis.

FUNDING

This work was supported by the National Science Foundation [OCE-0452401, EAR-0738880] and by the Woods Hole Oceanographic Institute Academic Program Office as part of a field class run by P.B.K. and G.H.

SUPPLEMENTARY DATA

Supplementary data for this paper are available at *Journal of Petrology* online.

REFERENCES

Ahern, J. L. & Turcotte, D. L. (1979). Magma migration beneath an ocean ridge. *Earth and Planetary Science Letters* **45**, 115–122.

Buck, W. R. & Su, S. (1989). Focused mantle upwelling below mid-ocean ridges due to feedback between viscosity and melting. *Geophysical Research Letters* **16**, 641–644.

Cooper, R. F. & Kohlstedt, D. L. (1982). Interfacial energies in the olivine–basalt system. In: Akimoto, S. & Manghnani, M. H. (eds) *High Pressure Research in Geophysics, Advances in Earth and Planetary Science*. Tokyo: Academic Publications, pp. 217–228.

Dick, H. J. B. (1977*a*). Partial melting in the Josephine peridotite; I, The effect of mineral composition and its consequence for geobarometry and geothermometry. *American Journal of Science* **277**, 801–832.

Dick, H. J. B. (1977*b*). Evidence of partial melting in the Josephine Peridotite. In: Dick, H. J. B. (ed.) *Magma Genesis, Proceedings of the American Geophysical Union Chapman Conference on Partial Melting in the Earth's Upper Mantle*. Portland: Oregon Department of Geology and Mineral Industries, pp. 59–62.

Dunn, R. A. & Forsyth, D. W. (2003). Imaging the transition between the region of mantle melt generation and the crustal magma chamber beneath the southern East Pacific Rise with short-period Love waves. *Journal of Geophysical Research, B, Solid Earth and Planets*.

Faul, U. H. (1997). Permeability of partially molten upper mantle rocks from experiments and percolation theory. *Journal of Geophysical Research, B, Solid Earth and Planets* **102**, 10299–10311.

Faul, U. H. (2001). Melt retention and segregation beneath mid-ocean ridges. *Nature* **410**, 920–923.

Faul, U. H., Toomey, D. R. & Waff, H. S. (1994). Intergranular basaltic melt is distributed in thin, elongated inclusions. *Geophysical Research Letters* **21**, 29–32.

Gribb, T. T. & Cooper, R. F. (2000). The effect of an equilibrated melt phase on the shear creep and attenuation behavior of polycrystalline olivine. *Geophysical Research Letters* **27**, 2341–2344.

Harper, G. D. (1984). The Josephine ophiolite, northwestern California. *Geological Society of America Bulletin* **95**(9), 1009–1026.

Hess, P. C. (1989). *Origins of Igneous Rocks*. Cambridge, MA: Harvard University Press, 336 p.

Hiraga, T., Anderson, I. M. & Kohlstedt, D. L. (2003). Chemistry of grain boundaries in mantle rocks. *American Mineralogist* **88**, 1015–1019.

Hirth, G. & Kohlstedt, D. L. (2003). Rheology of the upper mantle and the mantle wedge: a view from the experimentalists. In: Eiler, J. (ed.) *Inside the Subduction Factory. Geophysical Monograph, American Geophysical Union* **138**, 83–105.

Holtzman, B. K. *et al.* (2003). Stress-driven melt segregation in partially molten rocks. *Geochemistry, Geophysics, Geosystems* **4**(5), doi:10.1029/2001GC000258.

Iwamori, H. (1993*a*). A model for disequilibrium mantle melting incorporating melt transport by porous and channel flows. *Nature* **366**, 734–737.

Iwamori, H. (1993*b*). Dynamic disequilibrium melting model with porous flow and diffusion-controlled chemical equilibration. *Earth and Planetary Science Letters* **114**, 301–313.

Johnson, K. T. M., Dick, H. J. B. & Shimizu, N. (1990). Melting in the oceanic upper mantle: an ion microprobe study of diopsides in abyssal peridotites. *Journal of Geophysical Research* **95**(B3), 2661–2678.

Jung, H. & Waff, H. S. (1998). Olivine crystallographic control and anisotropic melt distribution in ultramafic partial melts. *Geophysical Research Letters* **25**, 2901–2904.

Kelemen, P. B. (1986). Assimilation of ultramafic rock in subduction-related magmatic arcs. *Journal of Geology* **94**, 829–843.

Kelemen, P. B. (1990). Reaction between ultramafic rock and fractionating basaltic magma. I. Phase relations, the origin of calc-alkaline magma series, and the formation of discordant dunite. *Journal of Petrology* **31**, 51–89.

Kelemen, P. B. & Dick, H. J. B. (1995). Focused melt flow and localized deformation in the upper mantle: Juxtaposition of replacive dunite and ductile shear zones in the Josephine peridotite, SW Oregon. *Journal of Geophysical Research* **100**(B1), 423–438.

Kelemen, P. B., Hirth, G., Shimizu, N., Spiegelman, M. & Dick, H. J. B. (1997). A review of melt migration processes in the adiabatically upwelling mantle beneath oceanic spreading centers. *Philosophical Transactions of the Royal Society of London* **355**, 283–318.

Loney, R. A. & Himmelberg, G. R. (1976). Structure of the Vulcan Peak alpine-type peridotite, southwestern Oregon. *Geological Society of America Bulletin* **87**, 259–274.

Lundstrom, C. C., Gill, J., Williams, Q. & Perfit, M. R. (1995). Mantle melting and basalt extraction by equilibrium porous flow. *Science* **270**(5244), 1958–1961.

Lundstrom, C. C., Gill, J. & Williams, Q. (2000). A geochemically consistent hypothesis for MORB generation. *Chemical Geology* **162**, 105–126.

McKenzie, D. (1984). The generation and compaction of partially molten rock. *Journal of Petrology* **25**, 713–765.

McKenzie, D. (1989). Some remarks on the movement of small melt fractions in the mantle. *Earth and Planetary Science Letters* **95**(1–2), 53–72.

Morgan, Z., Liang, Y. & Kelemen, P. (2008). Significance of the concentration gradients associated with dunite bodies in the Josephine and Trinity ophiolites. *Geochemistry, Geophysics, Geosystems* **9**, Q07025, doi:10.1029/2008GC001954.

Nicolas, A. (1986). A melt extraction model based on structural studies in mantle peridotite. *Journal of Petrology* **27**, 999–1022.

Philip, S., Jessica, M. W., Peter, B. K. & Greg, H. (2009). Microstructural and rheological evolution of a mantle shear zone. *Journal of Petrology* , doi:10.1093/petrology/egp057.

Quick, J. E. (1982). The origin and significance of large, tabular dunite bodies in the Trinity perioditite, northern California. *Contributions to Mineralogy and Petrology* **78**, 413–422.

Renner, J., Viskupic, K., Hirth, G. & Evans, B. (2003). Melt extraction from partially molten peridotites. *Geochemistry Geophysics, Geosystems* **4**, doi:10.1029/2002GC000369.

Roberts, J. J. & Tyburczy, J. A. (1998). Partial-melt electrical conductivity: Influence of melt composition. *Journal of Geophysical Research* **104**(B4), 7055–7065.

Scott, D. R. & Stevenson, D. J. (1986). Magma ascent by porous flow. *Journal of Geophysical Research* **91**, 9283–9296.

Skemer, P., Warren, J. M., Kelemen, P. B. & Hirth, G. (2009). Microstructural and Rheological Evolution of a Mantle Shear Zone. *Journal of Petrology* **51**, 43–53.

Sleep, N. H. (1974). Segregation of magma from a mostly crystalline mush. *Geological Society of America Bulletin* **85**, 1225–1232.

Spiegelman, M. (1996). Geochemical consequences of melt tranport in 2-D: The sensitivity of trace elements to mantle dynamics. *Earth and Planetary Science Letters* **139**, 115–132.

Toramaru, A. & Fujii, N. (1986). Connectivity of melt phase in partially molten peridotite. *Journal of Geophysical Research* **91**, 9239–9252.

Turcotte, D. L. & Phipps Morgan, J. (1992). The physics of magma migration and mantle flow beneath a mid-ocean ridge. In: Phipps Morgan, J., Blackman, D. K. & Sinton, J. M. (eds) *Mantle Flow and Melt Generation at Mid-Ocean Ridges. Geophysical Monograph, American Geophysical Union* **71**, 155–182.

Turcotte, D. L. & Schubert, G. (2002). *Geodynamics*, 2nd edn edn. Cambridge: Cambridge University Press, 456 p.

Von Bargen, N. & Waff, H. S. (1986). Permeabilities, interfacial areas, and curvatures of partially molten systems; results of numerical computations of equilibrium microstructures. *Journal of Geophysical Research* **91**, 9261–9276.

Waff, H. S. & Bulau, J. R. (1979). Equilibrium fluid distribution in an ultramafic partial melt under hydrostatic stress conditions. *Journal of Geophysical Research* **84**, 6109–6114.

Waff, H. S. & Faul, U. H. (1992). Effects of crystalline anisotropy of fluid distribution in ultramafic partial melts. *Journal of Geophysical Research* **97**, 9003–9014.

Wan, Z., Coogan, L. A. & Canil, D. (2008). Experimental calibration of aluminum partitioning between olivine and spinel as a geothermometer. *American Mineralogist* **93**, 1142–1147.

Wark, D. A. & Watson, E. B. (1998). Grain-scale permeabilities of texturally equilibrated, monomineralic rocks. *Earth and Planetary Science Letters* **164**, 591–605.

Wark, D. A., Williams, C. A., Watson, E. B. & Price, J. D. (2003). Reassessment of pore shapes in microstructurally equilibrated rocks, with implications for permeability of the upper mantle. *Journal of Geophysical Research, B, Solid Earth and Planets*, doi: 10.1029/2001JB001575.

Warren, J. M., Hirth, G. & Kelemen, P. B. (2008). Evolution of olivine lattice preferred orientation during simple shear in the mantle. *Earth and Planetary Science Letters* **272**, 501–512.

Zhu, W. & Hirth, G. (2003). A network model for permeability in partially molten rocks. *Earth and Planetary Science Letters* **212**, 407–416.

Zimmerman, M. E., Zhang, S., Kohlstedt, D. L. & Karato, S.-i. (1999). Melt distribution in mantle rocks deformed in shear. *Geophysical Research Letters* **26**(10), 1505–1508.